Journal of Solid State Chemistry **168,** 41–51 (2002)
doi:10.1006/jssc.2002.9676

Crystal Structures and Magnetic Properties of the Two Misfit Layer Compounds: $[SrGd_{0.5}S_{1.5}]_{1.16}NbS_2$ and $[Sr(Fe,Nb)_{0.5}S_{1.5}]_{1.13}NbS_2$

O. Leynaud, A. Lafond, Y. Moëlo, P. Palvadeau, and A. Meerschaut[1]

Institut des Matériaux Jean Rouxel, Laboratoire de Chimie des Solides, UMR-CNRS 6502, 2 rue de la Houssinière, BP 32229, 44322 Nantes cedex 03, France

Received February 19, 2002; in revised form May 22, 2002; accepted May 28, 2002

Crystal structures of two new misfit compounds, $[SrGd_{0.5}S_{1.5}]_{1.16}NbS_2$ and $[Sr(Fe,Nb)_{0.5}S_{1.5}]_{1.13}NbS_2$, were determined through the composite approach, i.e., by refining each subpart (*Q*, *H*-parts, and the common part) of these composite materials, separately. The *Q*-part is a three-atom-thick layer, with the NaCl-type structure, where external SrS planes enclose the inner GdS or (Fe,Nb)S plane; the structural difference between these two compounds lies in the central layer within the *Q*-part: Gd and S atoms are in special positions (octahedral coordination), while Fe and S atoms are statistically distributed on split (×4) positions (tetrahedral coordination) around a central unique site (= special position occupied by Nb). The *H*-part is a sandwich of sulfur planes enclosing the inner Nb plane as observed for the structure of the binary compound NbS_2 itself. The Sr–Gd derivative shows a paramagnetic behavior in the whole studied temperature range (2–300 K). On the other hand, antiferromagnetic interactions occur in the Sr–Fe derivative; the complex magnetic behavior of this compound is related to the statistical distribution of Fe atoms which leads to frustration of the magnetic interactions. At room temperature, experimental values obtained from Mössbauer spectrum correspond to Fe^{3+} in tetrahedral sulfur environment: isomer shift $\delta = 0.32\,mm\,s^{-1}$, and quadrupole splitting $\Delta E = 0.48\,mm\,s^{-1}$.

Key Words: **crystal structure; 2D-misfit; sulfide; magnetism; Mössbauer.**

INTRODUCTION

The study of the synthetic misfit layer compounds $[(MX)_m]_{1+x}[TX_2]_n$, where M = rare earth, Sn, Pb, Sb, Bi; T = Ti, V, Cr, Nb, Ta; X = S, Se; m = 1, 2 and n = 1, 2, 3, was primarily focused on the recognition of various stacking sequences, defined by the m/n ratio, that would exist in this family of compounds (1, 2). The former known synthetic misfit compounds corresponded to the monolayer-type structure ($n = 1$; $m/n = 1/1$), i.e., an alternate stacking of the $[MX]$ part ($= Q$) and the $[TX_2]$ part ($= H$); in accordance with the International symbols for crystal systems (3), Q and H refer to tetragonal and hexagonal symmetries, respectively. The family of misfit compounds was then enlarged to the bilayer type ($n = 2$) (4) and even up to the trilayer type ($n = 3$) (5, 6), i.e., with multiple H layers. The stacking sequence corresponding to the $m/n = 2/1$ ratio was recently encountered for a Pb/Sb misfit derivative of the natural franckeite type (7). But the most recent novelty refers to the characterization of a new member, labeled the $1.5Q/1H$ homolog (8, 9). The structure of its Q-subpart is a three-atom-thick layer, which differs from an even-atom-thick one as this occurred in all the previous $1Q$ or $2Q$ misfit parents. As a direct consequence, the situation of atoms in the median plane is not equivalent to that of atoms located on the surfaces for this "1.5 Q-slab". This authorizes either a difference between metal atoms occupying these sites, as for instance Fe in the central part and Pb at the border (8), or the same kind of metal atom but at different oxidation states as noticed with europium (occurrence of a mixed valence states: 2 Eu^{2+} (external sheets) for 1 Eu^{3+} (central sheet)) (9). The structure of the Pb–Fe $1.5Q$-derivative shows that Fe atoms occupy a four-split position (distorted tetrahedral site) close around the central one (compressed octahedral site) also occupied by Fe (and minor Nb). Because of the very large absorption coefficient of the Pb element which had interfered with Mössbauer studies, we decided to prepare the Sr-substituted phase (Sr–Fe compound) to better analyze the situation of iron atoms. After this, and because of the complexity of the Fe–site distribution, we also prepared another material (Sr–Gd), with Gd^{3+} ion substituting Fe^{3+} in the median plane, knowing that only a single site (central site = octahedral) was observed in the corresponding Eu-$1.5Q$-derivative (9). This paper deals with syntheses and chemical analyses of these two Sr–Fe

[1] To whom correspondence should be addressed. Fax: 33 2 40 37 3995. E-mail: alain.meershaut@cnrs–imn.fr.

0022-4596/02 $35.00

and Sr–Gd misfit compounds, their structure determinations, and their magnetic properties coupled with a Mössbauer study on the Sr–Fe member.

EXPERIMENTAL

Syntheses

For the Sr–Fe phase, a mixture of SrS, Fe, Nb, and S, in the respective 1.16:0.58:1.00:2.58 ratios, was introduced into a silica tube sealed under vacuum ($p \approx 2 \times 10^{-2}$ bar). The temperature was progressively raised ($10^{\circ}C\,h^{-1}$) up to 1000°C after two steps of 24 h at 400°C and 700°C. Then, the temperature was kept constant at 1000°C during 1 week; finally, the furnace was shut off and allowed to cool.

For the Sr–Gd phase, the starting materials SrS, Gd_2S_3, Nb, and S were mixed in the ratios 1.16:0.29:1.00:1.71, respectively; iodine ($5\,mg \cdot cm^{-3}$) was also added in this initial stage. Gd_2S_3 is home-made by the sulfurization of Gd_2O_3 under a gas flow of H_2S at 1200°C during 8 h. The same heating process as for the synthesis of the Sr–Fe phase was applied.

Chemical Analysis

Synthetic products were mounted in epoxy, then prepared as polished sections, to permit their detailed observation through reflected light microscopy, and their examination with scanning electron microscope (SEM) equipped with energy dispersive spectrometer (EDS). Such a qualitative approach is essential to detect possible additional phases present as traces (below detection limit of X-ray powder diffraction), which could distort magnetic measurements.

SEM-EDS analysis of the Sr–Gd compound gave a composition quite in agreement with the structural resolution. The mean of 42 spot analyses gave (wt%): Sr 23.3(7), Gd 22.3(5), Nb 24.9(5), S 31.9(5), sum 102.4(1.4). On the basis of S = 3.74 atoms, it gives the structural formula $[Sr_{0.94}Gd_{0.48}S_{1.5}]_{1.16}Nb_{1.05}S_2$. The Sr–Fe compound revealed a more complex chemistry, due to the incorporation of an Nb excess in the *Q* layer, like for previous homologous compounds Pb–Fe and Pb–Mn (8). Various synthetic samples from different batches were thus precisely analyzed with an electron microprobe equipped with a wavelength dispersive spectrometer (WDS) (CAMECA SX 50 apparatus; BRGM-CNRS-University common laboratory, Orléans). Operating conditions were as follows: accelerating voltage 15 kV; beam current 20 nA; standards (element, *emission line*): pyrite FeS_2 (S$K\alpha$ and Fe$K\alpha$), $SrSO_4$ (Sr$L\alpha$) and Nb metal (Nb$L\alpha$); counting time/element 10 s.

Analysis of the sample from which the crystal used for the structural study was picked, gave the following composition (wt%—mean of 28 spot analyses): Sr 27.9(6), Fe 6.9(1), Nb 30.7(3), S 34.7(2), sum 100.2(6). On the basis of S = 3.695 atoms (fixed by crystallographic data), one obtains the atomic coefficients $Sr_{1.088}$ $Fe_{0.423}$ $Nb_{1.130}$ $S_{3.695}$, which allow to propose the chemical structural formula: $[Sr_{0.963}(Fe_{0.374}Nb_{0.115})_{\Sigma=0.489}S_{1.5}]_{1.13}$ NbS_2.

A similar composition was obtained in another sample where the compound $Fe_{1/3}NbS_2$ was also present. It gave (wt%—mean of two spot analyses): Sr 25.2, Fe 8.4, Nb 31.2, S 34.7, sum 99.4; structural formula: $[Sr_{0.87}(Fe_{0.45}Nb_{0.13})_{\Sigma=0.58}S_{1.5}]_{1.13}$ NbS_2. There is clearly an increase of Fe content, in accordance with the formation of $Fe_{1/3}NbS_2$ in excess. Other samples gave a very homogeneous composition, but with a lower Me/S ratio. Without precise structural data, it is not possible to explain this chemical shift relatively to the first one. A typical composition is (wt%—mean of 40 spot analyses): Sr 25.5(5), Fe 7.0(2), Nb 31.6(3), S 35.9(4), sum 99.9(5), leading to the chemical formulation: $[Sr_{0.851}(Fe_{0.366}Nb_{0.108})_{\Sigma=0.474}S_{1.5}]_{1.13}$ NbS_2.

Data Collection

The platelet-shaped crystals with dimensions $0.07 \times 0.06 \times 0.02\,mm^3$ for the Sr–Fe crystal, and $0.11 \times 0.06 \times 0.01\,mm^3$ for the Sr–Gd one, were mounted on an Imaging Plate diffractometer (IPDS STOE) using the Mo$K\alpha$ radiation ($\lambda = 0.71073$ Å). The crystal-to-detector distances were set to 70 mm for Sr–Fe and to 80 mm for Sr–Gd; 250 exposures ($0 < \varphi < 200^{\circ}$, $\Delta\varphi = 0.8^{\circ}$) and 200 exposures ($0^{\circ} < \varphi < 200^{\circ}$, $\Delta\varphi = 1^{\circ}$) were processed with the set of program from STOE (10), for the two records, respectively. The conditions of the data collections as well as structure details for both compounds are summarized in Table 1. All calculations were performed with the JANA98 chain programs (11).

STRUCTURAL DETERMINATION

Although the true and complete structure solution for the so-called incommensurate inter-growth compounds can only be provided, ultimately, by the super-space approach (12–16), we neglected its use for some reasons, the main one being the poor quality of the studied crystals conjugated with the absence of satellite spots. However, it has to be recalled that such a structural approach was previously implemented for the parent $1.5Q/1H$ compound $[(EuS)_{1.5}]_{1.15}NbS_2$ (9), which exactly corresponded to the example of the Sr–Gd derivative, considering their unit-cell parameters as well as their respective subspace groups; the good quality of the Eu-studied crystal had authorized such a study, in the super-space group $G_s = Fm2m(\alpha, 0, 0)$ with $\alpha = 0.5768$; refinement converged to very low *R* values

TABLE 1
Data Collection Conditions and Refinement Results

Empirical formula	$[SrGd_{0.5}S_{1.5}]_{1.16}NbS_2$	$[Sr(Fe,Nb)_{0.5}S_{1.5}]_{1.13}NbS_2$
Crystal dimensions	$0.07 \times 0.06 \times 0.02\,mm^3$, bounded by {1 0 0}, {0 1 0}, {0 0 1}, respectively	$0.11 \times 0.06 \times 0.01\,mm^3$, bounded by {1 0 0}, {0 1 0}, {0 0 1}, respectively
Absorption correction	Faces-indexed option; $\mu = 20.48\,mm^{-1}$	Faces-indexed option; $\mu = 15.83\,mm^{-1}$
Density	$\rho = 4.8\,g\,cm^{-3}$	$\rho = 4.16\,g\,cm^{-3}$
Diffractometer	IPDS STOE	IPDS STOE
Radiation	Mo$K\alpha$ ($\lambda = 0.71069$ Å)	Mo$K\alpha$ ($\lambda = 0.71069$ Å)
Crystal-to-detector (IP), 2θ limit	80 mm, 48.4°	70 mm, 52.1°
	Refinement results	
Q part	Formula: Sr_2GdS_3; $Z = 2$	Formula: $Sr_2(Fe_{0.79},Nb_{0.21})S_3$; $Z = 4$
Cell parameters (Å)	$a = 5.7565(8)$, $b = 5.7822(9)$, $c = 14.917(3)$	$a = 5.8920(9)$, $b = 5.8369(8)$, $c = 28.076(6)$
Symmetry	Orthorhombic	Orthorhombic
Space group	*Cm2m*	*Fm2m*
Indice range collection h,k,l	−6, 6; −6, 6; −16, 17	−7, 6; −7, 6; −34, 33
Absorption correction Tmin/Tmax	0.33/0.67	0.29/0.85
Number of reflections $I \geq 3\sigma(I)$	243	251
Number of refined parameters	15	23
Reliability factors R^a, $R_w{}^a$	4.37, 4.67	4.37, 4.58
Largest peaks in Fourier difference	$+2.56\,e^-/Å^3$; $-2.40\,e^-/Å^3$	$+1.08\,e^-/Å^3$; $-1.54\,e^-/Å^3$
H part	Formula: NbS_2; $Z = 2$	Formula: NbS_2; $Z = 2$
Cell parameters (Å)	$a = 3.3301(5)$, $b = 5.7816(9)$, $c = 14.922(4)$	$a = 3.3246(5)$, $b = 5.8313(9)$, $c = 14.045(3)$
Symmetry	Orthorhombic	Orthorhombic
Space group	*Cm2m*	*Cm2m*
Indice range collection h,k,l	−3, 3; −6, 6; −16, 17	−4, 3; −6, 6; −17, 16
T_{min}/T_{max}	0.32/0.67	0.36/0.85
Number of reflections $I \geq 2\sigma(I)$	182	194
Number of refined parameters	10	10
Reliability factors R^a, $R_w{}^a$	4.94, 5.23	4.95, 5.29
Largest peaks in Fourier difference	$+2.37\,e^-/Å^3$; $-2.61\,e^-/Å^3$	$+4.10\,e^-/Å^3$; $-3.45\,e^-/Å^3$
Common part		
Space group	*c*11*m* (No. 6)	*c*11*m* (No. 6)
Number of reflections $I \geq 2\sigma(I)$	87	90
Number of refined parameters	7	9
Reliability factors R^a, $R_w{}^a$	9.97, 11.87	5.53, 5.61

$^a R = \sum(|F_{obs}|\text{-}|F_{calc}|)/\sum(F_{obs})$; $R_w = (\sum w(|F_{obs}|\text{-}|F_{calc}|)^2/\sum w(F_{obs})^2)^{1/2}$; $w = 1$.

R/R_w (%) = 3.58/4.75. Therefore, the modulated structure was known, and subsequently the inter-atomic distances at the interface between the *Q* and the *H*-parts. Then, under these conditions, the aim of the study of Sr–Gd and Sr–Fe compounds was rather to depict the situation about the *Q*-part for the two Sr–Gd and Sr–Fe structures, by comparison with the isotypic Eu-homolog. Indeed, magnetic and Mössbauer results are associated with Gd and Fe cations which belong to this *Q*-part, and are not concerned by the *Q*/*H* interface. Thus, the structure determinations were done in the composite approach, which means that each subpart of the structure (*Q* and *H*-parts) was solved separately, not forgetting to suppress the common reflections (0*kl*, **a** being the misfit direction) in both cases. These common reflections are later used to get the relative arrangement between *Q*- and *H*-parts, refining the *y* and *z* positional parameters of only one atom, all the other coordinates for the remaining atoms being "constrained in a riding mode"; indeed, in order to preserve the structure solutions found from the separate subsystem refinements, all the other atom parameters are adjusted to this reference atom.

The crystal structure of $[PbFe_{0.5}S_{1.5}]_{1.16}NbS_2$, which was also solved by the composite approach (8), has been taken as a model for the structure determination of the two new materials.

Refinement of the Q-part of the Sr–Fe and Sr–Gd Derivatives "Sr–Fe"

The existing conditions for *hkl* reflections are indicative of an *F*-centering for Sr–Fe (it is a *C*-centering for Sr–Gd). Among the five possible space groups *F*222 (No. 22), *Fmm*2-*Fm*2*m*-*F*2*mm* (No. 42), and *Fmmm* (No. 69), only

refinements in *Fm*2*m* and *Fmmm* gave satisfying results. As mentioned later in the text, the space group *Cm*2*m* for the *H*-part implies (see Refs. (14, 15)) an acentric space group for the *Q*-part too; thus, the space group *Fm*2*m* was chosen. We encountered the same situation as for the Pb–Fe compound (8) concerning the atomic positions within the median plane, i.e., a statistical distribution over split positions for both Fe and S atoms. However, according to the chemical analysis, the amount of iron is not large enough to justify a full-site occupancy of the split positions; on the contrary, result of the chemical analysis for the Nb content gives evidence that a fraction of Nb has to be involved in the *Q*-part. Based on the cation size or coordination, coupled with refinements for hypothetical atomic combinations, the central site was attributed to Nb exclusively, whereas the four split ones were occupied by Fe only, with the constraint that the sum of the site-occupancy factors (s.o.f) corresponds to a 100% occupied unique central position. This means that the Fe/Nb ratio was free to vary within this condition. The occupancy of this mixed site, $Fe_{0.77}Nb_{0.23}$, is very close to that obtained from the microprobe analysis, $Fe_{0.76}Nb_{0.24}$. An example for such a statistical Fe/Nb disorder, but on an octahedral site was reported for the Fe1 + *x*Nb3 − *x*Se10 compound (17). Correspondingly, S atoms are located on a four split positions (on the (8c) site: S21; *xy*0; on the (4a) site: S22a and S22b; 0*y*0 with $x, y \approx \pm 0.43$) around the central position (which would correspond to the (4b) site ($\frac{1}{2}$ 0 0) of the space group *Fmmm*). The final refinement on data corrected from absorption effect (face indexed option) yielded reliability factors $R = 4.37\%$ and $R_w = 4.58\%$, for 251 reflections ($I \geq 3\sigma(I)$) with 23 variables. The maximal and minimal densities in the last Fourier difference synthesis were $+1.08$ and $-1.54\,e^-\,A^{-3}$, respectively. Values of atomic coordinates and isotropic/anisotropic thermal parameters are given in Table 2.

"Sr–Gd"

Among the five possible space groups, namely *C*222 (No. 21), *Cmm*2 (No. 35), *Cm*2*m* and *C*2*mm* (*Amm*2 (No. 38)), and *Cmmm* (No. 65), the space group *Cm*2*m* was chosen for the same reasons as above (both acentric space groups for the *Q*- and *H*-parts). The resulting structure solution is comparable to that found for the $[(Eu_{1.5}S_{1.5})_{1.15}NbS_2$ homolog (9) (except for the *C*-centering instead of the *F*-centering), i.e., Sr atoms located on the external layers, sandwiching the central layer with Gd. For this solution, the Gd atoms as well as the S atoms constituting the median plane are both on the special 2a/2b positions, respectively, instead of split ones as observed for the Sr–Fe case.

The final refinement, after absorption corrections, converges to reliability factors $R = 4.37\%$ and $R_w = 4.67\%$ for 243 reflections ($I \geq 3\sigma(I)$) with 15 variables. The last Fourier difference calculation was featureless. Values of atomic coordinates and isotropic/anisotropic thermal parameters are given in Table 3.

Refinement of the H-Part of the Sr–Fe (i) and Sr–Gd (ii) Derivatives

For both structure determinations, refinements were conducted in the non-centrosymmetric space group *Cm*2*m* (= non-conventional space group, derived from *Amm*2 (No. 38) after *abc* → *bca* permutation). After performing absorption corrections using the face indexed option, and taking into account anisotropic thermal parameters for Nb and S atoms, the final refinement converged to reliability factors $R = 4.95\%$ and $R_w = 5.29\%$ for 194 reflections (($I \geq 2\sigma(I)$) with 10 variables for the Sr–Fe structure, and to $R = 4.94\%$ and $R_w = 5.23\%$ for 182 reflections (($I \geq 2\sigma(I)$) with 10 variables for the Sr–Gd structure; the highest peaks

TABLE 2
Fractional Atomic Coordinates (a) and Anisotropic Atomic Displacements (b) for the *Q*-part of Sr–Fe

(a)	Atom	mult.	s.o.f.	*x*	*y*	*z*	U_{iso}, U_{eq} [a]
	Sr	8d	1	0	0.487(8)	0.1051(2)	0.0175(4)[a]
	Nb	4a	0.227(16)	0	0	0	0.015(5)
	Fea	8c	0.193(−)	0.093(5)	0.100(8)	0	0.016(3)
	Feb	8c	0.193(−)	0.117(4)	−0.104(8)	0	0.016(3)
	S1	8d	1	0	−0.013(9)	0.0781(2)	0.0248(13)[a]
	S21	8c	0.25	0.430(3)	0.001(14)	0	0.022(4)
	S22a	4a	0.25	0	0.544(25)	0	0.022(−)
	S22b	4a	0.25	0	0.417(23)	0	0.022(−)
(b)	Atom	U_{11}	U_{22}	U_{33}	U_{12}	U_{13}	U_{23}
	Sr	0.0195(7)	0.0146(7)	0.0185(8)	0	0	0
	S1	0.015(2)	0.010(2)	0.050(3)	0	0	0

[a] U_{eq} is defined as one-third of the trace of the orthogonalized U_{ij} tensor.

TABLE 3
Fractional Atomic Coordinates (a) and Anisotropic Atomic Displacements (b) for the *Q*-Part of Sr–Gd

(a)	Atom	mult.	s.o.f.	x	y	z	U_{iso}, U_{eq}[a]
	Sr	4c	1	0	0.495(2)	0.2229(1)	0.0043(5)[a]
	Gd	2a	1	0	0	0	0.0162(5)[a]
	S1	4c	1	0	−0.007(4)	0.1824(3)	0.0126(8)
	S2	2a	1	0	0.497(4)	0	0.0134(11)
(b)	Atom	U_{11}	U_{22}	U_{33}	U_{12}	U_{13}	U_{23}
	Sr	0.0036(8)	−0.0005(10)	0.0097(9)	0	0	−0.001(4)
	Gd	0.0174(7)	0.0099(9)	0.0212(9)	0	0	0

in the final Fourier difference maps had a height of 4.10 and $2.37\,e^{-}/A^{-3}$, respectively. Table 4 lists the atomic coordinates for both compounds, together with the anisotropic thermal parameters.

Refinement of the Common Part of the Sr–Fe and Sr–Gd Derivatives

The relative arrangement of the two sublattices (*Q* and *H*-parts) was obtained from refinement of the $0kl$ reflections common to both parts. Intensities of these reflections were corrected for absorption effects.

Concerning the Sr–Fe derivative, the *Q*-part is related to an *F*-centered system ($c = 28.076$ Å), while the *H*-part is associated with a *C*-centered system ($c = 14.045$ Å). Consequently, the refinement of the common part was performed in the $c11m$ space group ($c = 14.045$ Å), ignoring the x coordinates. Results from the refinement of the separate *Q*-part were kept unchanged (except for the z coordinates which were multiplied by two because of the **c**/2 value of 14.045 Å). To adjust the *H*-part against the *Q*-part, only the y coordinate of Nb was set free, the y coordinate of the associated S atoms of the *H*-part being constrained to shift by an equal δy value ($=0.3323$) as refined in the separate NbS_2 part; the z coordinates for both Nb and S are fixed to their primitive values. Finally, the relative diffracting weight between the *Q*- and *H*-parts was fixed in agreement with the mismatch ratio $a_H/a_Q = 0.5643$; this normalizes the contribution of each part to the same volume. Following this, all the statistical occupancies that have been previously refined for Fe1 and Fe2 positions, as well as S21 and S22 ones, will be then multiplied by this factor. Under these conditions, the final refinement led to reliability factors $R = 5.53\%$ and $R_w = 5.61\%$ for 90 reflections ($(I \geq 2\sigma(I))$) with nine variables. Atomic coordinates and isotropic thermal parameters are reported in Table 5.

The Sr–Gd example is much simpler than the Sr–Fe one, first because both subparts are *C*-centered with the same **c**-parameter, and secondly because there are no statistical occupancies for any atoms within the *Q*-part. Referring to the same procedure as just described above for Sr–Fe, the

TABLE 4
Fractional Atomic Coordinates (a) and Anisotropic Atomic Displacements (b) for the *H*-Part of Sr–Gd and Sr–Fe

(a)	Atom	mult.	s.o.f.	x	y	z	U_{eq}
Sr–Gd							
	Nb	2b	1	0	0	$\frac{1}{2}$	0.0071(8)
	S3	4c	1	0	0.3325(9)	0.3955(3)	0.014(2)
Sr–Fe							
	Nb	2b	1	0	0	$\frac{1}{2}$	0.0065(6)
	S3	4c	1	0	0.3323(7)	0.3888(3)	0.0101(14)
(b)	Atom	U_{11}	U_{22}	U_{33}	U_{12}	U_{13}	U_{23}
Sr–Gd							
	Nb	0.0131(13)	0.0009(15)	0.0073(16)	0	0	0
	S3	0.014(2)	0.005(4)	0.022(4)	0	0	0.003(2)
Sr–Fe							
	Nb	0.0057(8)	0.0022(10)	0.0116(11)	0	0	0
	S3	0.0045(17)	0.006(2)	0.020(3)	0	0	0.0018(16)

TABLE 5
Fractional Atomic Coordinates and Isotropic Displacement Parameters for Sr–Fe: Common Part

Atom	s.o.f.	x	y	z	U_{iso}
Nb1	0.1496	—	0	0	0.03(3)
Fe1	0.1037		0.10033	0	0.021(8)
Fe2	0.1037	—	−0.10391	0	0.021(−)
Sr	0.5643	—	0.48725	0.21019	0.0160(13)
S1	0.5643	—	−0.01292	0.15618	0.020(4)
S21	0.148	—	0.00063	0	0.005(19)
S22	0.134	—	0.54435	0	0.005(−)
S23	0.134	—	0.41690	0	0.005(−)
Nb2	1	—	−0.0902(6)	$\frac{1}{2}$	0.0077(9)
S3	1	—	0.24213(−)	0.38875	0.0113(15)

final refinement led to reliability factors $R = 9.97\%$ and $R_w = 11.87\%$ for 87 reflections ($(I \geq 2\sigma(I))$ with seven variables. Atomic positions and isotropic thermal parameters are reported in Table 6.

DESCRIPTION OF THE STRUCTURES

Figure 1 shows the projection of the whole structure of the Sr–Gd derivative onto the (b, c) plane such as resulting from the refinement of the common part. Whatever the example of the Q-part (for the Sr–Gd case or the Sr–Fe one), Sr atoms are always located on the external planes and are coordinated with five close S neighbors within this part as well as one to three (variable number in relation with the modulated character of the true structure) other S atoms belonging to the H-part.

Concerning the Sr–Gd derivative, one observes four planar Sr–S1 distances ($2 \times 2.941(1)$ Å, 2.96(3) and 2.94(3) Å), and one longer apical Sr–S2 distance (3.325(1) Å) within the Q-part; Sr–S distances with S atoms from the H-part can only be marked out because of the composite approach, typically from 2.9 Å (when $\delta x = 0$) to 4.1 Å ($\delta x = \frac{1}{2}$). However, as reported by van Smaalen using the super-space approach (14, 15) through the example of $(LaS)_{1.14}NbS_2$: "the modulation increases the distance at

TABLE 6
Fractional Atomic Coordinates and Isotropic Displacement Parameters for Sr–Gd: Common Part

Atom	s.o.f.	x	y	z	U_{iso}
Sr	0.5785	—	0.49511	0.22288	0.0115(13)
Gd	0.5785	—	0	0	0.025(2)
S1	0.5785	—	−0.00664	0.18237	0.008(3)
S2	0.5785	—	0.49740	0	0.008(−)
Nb	1	—	−0.0813(7)	$\frac{1}{2}$	0.0076(11)
S3	1	—	0.2512(−)	0.39548	0.014(2)

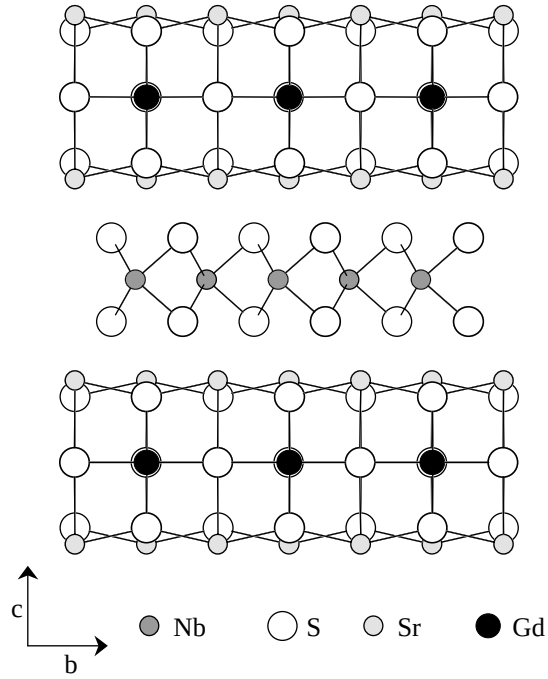

FIG. 1. Projection of the $1.5Q/1H$ misfit structure of Sr–Gd along the misfit direction.

closest approach between the subsystems, while it diminishes the variation of the shortest distance "(15). In the central Gd–S layer, Gd and S atoms are in octahedral coordination (apical distances: Gd–2S1 = 2.721(4) Å, and planar distances: Gd–4S2 = $2 \times 2.8783(2)$ Å, 2.91(4) and 2.88(4) Å); the octahedron is thus slightly compressed in the **c**-direction.

The structure of the Q-part for the Sr–Fe derivative (Fig. 2b) is very comparable to that of the Sr–Gd derivative (Fig. 2a) although a significant difference exists between them, considering the central layer level (compare Figs. 2a and 2b). Indeed, as discussed above, metal atoms (Fe,Nb) are distributed over a five-split position, i.e., a central site (Nb) with an octahedral environment coordinating (two shorter apical distances Nb–S1 = 2.194(5) Å, with the four closest planar distances Nb–2S21 = 2.529(16) Å, Nb–S22b = 2.43(13) and Nb–S22a = 2.66(14) Å), and four close positions (Fe) for a tetrahedral coordination. Because of the split Fe and S positions, the Fe–S distances can be gathered in groups of four distances, each Fe position ($2 \times$ Fe(a) and $2 \times$ Fe(b)) being in connection with two groups of S atoms labeled a,b,c,d, and a′,b′,c′,d′ for the shortest Fe–S distances, as indicated by the straight lines ($d < 2.9$ Å), and two groups of S atoms for much longer distances ($d > 3.15$ Å)(see Fig. 3). Among these eight shortest Fe–S distances (because of the statistical distribution of S atoms), only two of them must occur, and more precisely

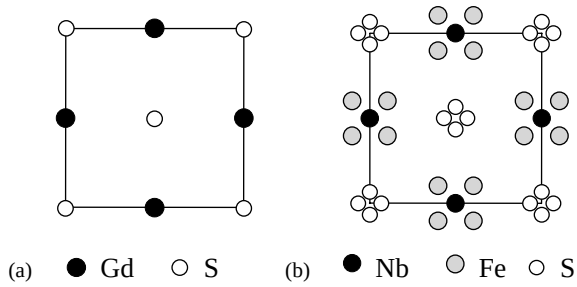

FIG. 2. Central layer (*ab* plane) of Sr–Gd (a) and Sr–Fe (b).

one among the a,b,c,d sites and another one among the a′,b′,c′,d′ sites; intermediate bond values (around 2.4 Å) are the most probable for an Fe–S contact with Fe^{3+} in a tetrahedral coordination. Each Fe atom (a and b) is close to two S1 atoms located along the **c**-axis at ≈ 2.35 Å. Table 7 summarizes selected Sr–S and Fe–S distances as well as Gd–S ones.

The structure of the *H*-part for both compounds is essentially the same as for the homolog $1Q/1H$ misfit compound, or that for a single slab of the binary NbS_2 itself, which means Nb atoms are in a trigonal prismatic coordination with S atoms. The calculated Nb–S distances agree very well with those mentioned in the literature ($6 \times$ Nb—S ≈ 2.48 Å).

MAGNETIC MEASUREMENTS

The magnetic susceptibility of both compounds was measured with a SQUID magnetometer (Quantum Design) between 2 and 300 K in a field of 1.0×10^{-2} T for the Gd sample and between 2 and 380 K in a field up to 0.100 T for the Fe sample, under field-cooled (FC) and zero-field cooled (ZFC) conditions. The samples were in a powder form for Sr–Gd, and a collection of small crystals for Sr–Fe. Raw data were corrected for the contribution of the sample holder, after which the diamagnetism of the core electrons was subtracted from the M/H ratio, yielding the magnetic dc-susceptibility.

Figure 4 shows the thermal variation of the magnetic susceptibility and its inverse for Sr–Gd. The linear variation of the inverse susceptibility can be modeled by a Curie–Weiss behavior ($\chi = C/(T-\theta)$) leading to a molar Curie constant of 7.82 emu K(mol Gd)$^{-1}$, which is comparable to the expected value for Gd^{3+} (7.88 emu K (mol Gd)$^{-1}$ or equivalently 9.90×10^{-5} m^3 K (mol Gd)$^{-1}$, with $S = J = \frac{7}{2}$ and $g_J = 2$). At very low temperatures, the susceptibility curve shows a very slight bending that could give notice of a magnetic transition of antiferromagnetic type, as suspected from the Weiss temperature $\theta = -6$ K (see inset of Fig. 4).

TABLE 7
Some Selected Distances for *Q*-Parts of Sr–Gd and Sr–Fe

"Sr–Gd"

Distances with Gd	*d* (Å)	SO[a]	Distances with Sr	*d* (Å)	SO[a]
$2 \times$ S1	2.721(4)	#1	$2 \times$ S1	2.9410(8)	#9
$2 \times$ S2	2.8783(2)	#4	S1	2.96(3)	#4
S2	2.88(4)	#1	S1	2.94(3)	#1
S2	2.91(4)	#4	S2	3.325(1)	#1

"Sr–Fe"

Distances with Nb	*d* (Å)	SO[a]	Distances with Fea	*d* (Å)	SO[a]
$2 \times$ S1	2.193(4)	#2	$2 \times$ S1	2.35(2)	#1
$1 \times$ S21	2.53(2)	#1	S22a (a)	2.42(4)	#8
$1 \times$ S21	2.53(2)	#2	S22b (b)	2.63(6)	#8
$1 \times$ S22b	2.43(13)	#1	S21 (c)	2.06(4)	#1
$1 \times$ S22a	2.66(14)	#4	S21 (d)	2.87(4)	#3
			S22a (a′)	2.65(15)	#1
Distances with Sr			S22b (b′)	1.93(14)	#1
$2 \times$ S1	3.0154(13)	#1	S21 (c′)	2.53(9)	#6
$2 \times$ S1	3.0420(13)	#6	S21 (d′)	2.34(9)	#7
$1 \times$ S21	2.981(4)	#6	(a,b,c,d) from Fig. 3		
$1 \times$ S22	2.98(2)	#1			
			Distances with Feb		
			$2 \times$ S1	2.36(2)	#1
			S22a (a)	2.41(6)	#8
			S22b (b)	2.26(3)	#8
			S21 (c)	1.94(4)	#1
			S21 (d)	2.74(4)	#3
			S22a (a′)	2.17(14)	#4
			S22b (b′)	2.88(14)	#4
			S22 (c′)	2.56(9)	#9
			S22 (d′)	2.32(9)	#10
			(a′,b′,c′,d′) from Fig. 3		

[a] SO, symmetry operations: #1 x,y,z; #2 $-x,-y,-z$; #3 $1-x,-y,-z$; #4 $x,-1+y,z$; #5 $-x,1-y,-z$; #6 $-\frac{1}{2}+x$, $\frac{1}{2}+y,z$; #7 $\frac{1}{2}-x$, $\frac{1}{2}+y,-z$; #8 $\frac{1}{2}+x,-\frac{1}{2}+y,z$; #9 $-\frac{1}{2}+x,-\frac{1}{2}+y,z$, #10 $-\frac{1}{2}+x$, $-\frac{1}{2}+y,-z$.

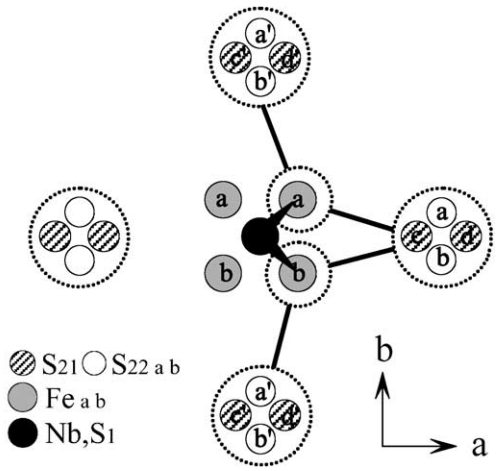

FIG. 3. Schematic view of the various planar Fe–S distances within the central layer of the *Q*-part, for the Sr–Fe derivative: there are two groups of four short Fe–S distances (named S) and two groups of four longer Fe–S distances (L).

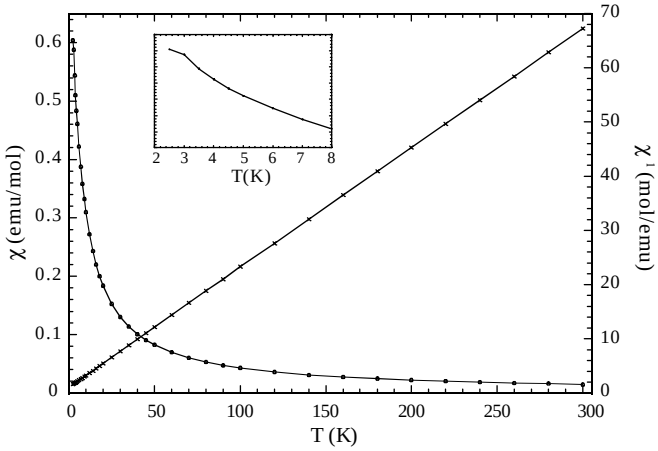

FIG. 4. Susceptibility and inverse susceptibility versus temperature for Sr–Gd.

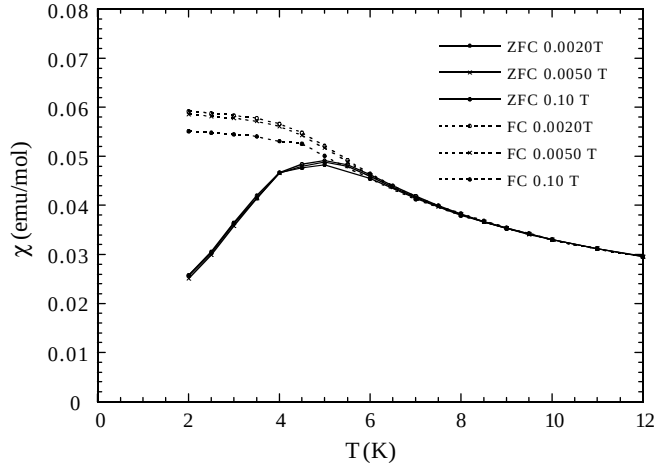

FIG. 6. Low-temperature ZFC and FC susceptibility for Sr–Fe.

Figure 5 shows the temperature dependence of the inverse susceptibility for Sr–Fe. There is a large downward curvature with no evidence of a linear domain in a large temperature range. Attempts to fit the high-temperature data (250–380 K) with a Curie–Weiss law failed because one obtains a Curie constant of $7.8\,\text{emu K(mol Fe)}^{-1}$, which is far above the spin-only value expected for Fe^{3+} ($4.38\,\text{emu K(mol Fe)}^{-1}$ or equivalently $5.50\times10^{-5}\,\text{m}^3\,\text{K (mol Fe)}^{-1}$), and a Weiss temperature of $\theta\approx-700\,\text{K}$. The low-temperature (2–12 K) thermal variation of the susceptibilities under various fields, and for both ZFC and FC conditions, are shown in Fig. 6. The ZFC curves show a maximum at about 5 K. The existence of a magnetic hysteresis indicates that some of the magnetic moments are blocked (frozen) during the ZFC process. These hysteresis phenomena below T_N, coupled with the fact that the extrapolated θ temperature shows a very large value ($|\theta|\approx700\,\text{K}$) compared to $T_N\approx5\,\text{K}$ would indicate that frustrated magnetic interactions are likely occurring in this material.

Frustration on a square antiferromagnetic lattice happens when the second-nearest-neighbor interactions, J2, exactly compensate the nearest-neighbor interactions, J1; in the real system, there is a distribution in the magnitude of these magnetic interactions due to the statistical distribution of the magnetic atoms over five sites. Such an explanation was already put forward for a similar magnetic behavior of the parent $[PbFe_{0.5}S_{1.5}]_{1.16}NbS_2$ compound (18). In order to better describe the magnetic frustrated state at low temperatures, *ac*-susceptibility measurements were carried out on the same SQUID magnetometer. The frequency band is between 10^3 and 10^{-3} Hz, but the very low amount of product did not allow us to measure below 1 Hz (see Fig. 7). Thus, four measurements were performed

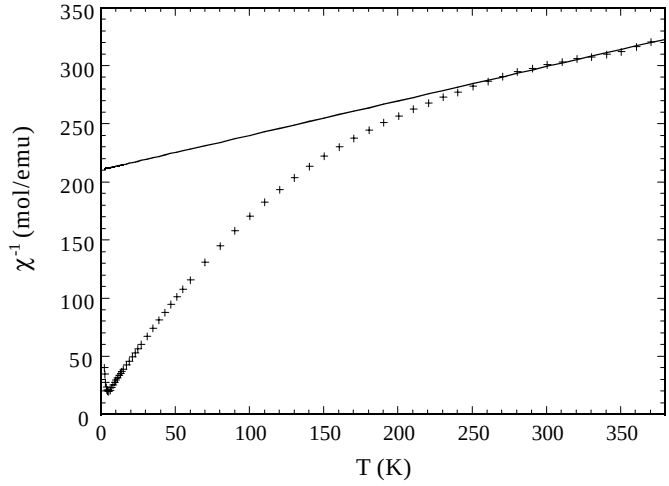

FIG. 5. Inverse susceptibility versus temperature for Sr–Fe.

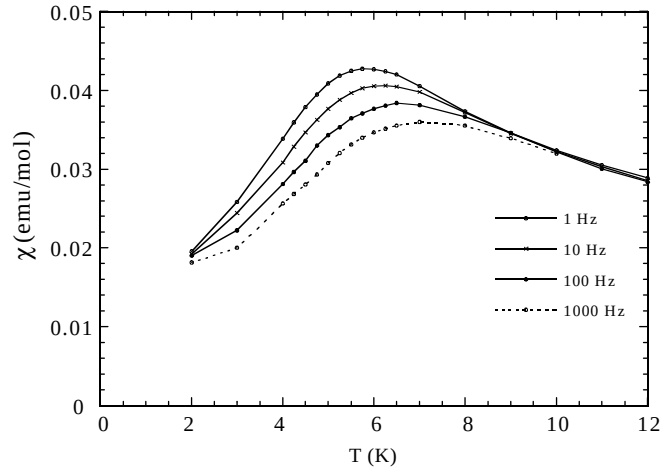

FIG. 7. *ac*-suceptibility for Sr–Fe.

at 1000, 100, 10 and 1 Hz, the value for the oscillating field acting on the sample being of 3×10^{-4} T. One observes a shift of T_{max} towards a higher temperature when the frequency is increased; this feature could correspond to either a spin-glass behavior, or a superparamagnetic one; both hypotheses were investigated using interpretations from (19):

for a spin-glass system, T_g (the glass temperature$\equiv T_{max}$, as labeled just before) shifts with the measuring frequency according to the equation: $T_g(t) = T_c(1 + (\tau_0/t)^{1/zv})$ (Eq. [1]);

for a super-paramagnetic system, the susceptibility again shows a cusp at T_b (blocking temperature$\equiv T_{max}$); the analog of (Eq. [1]) is: $T_b(t) = \varepsilon/(k_B \ln t/\tau_0)$ (Eq. [2]), with ε = energy barrier.

Experimentally, the frequency effect can be quantified in terms of a K parameter such as: $K = \Delta T_g/[T_g \Delta \log_{10}(f)]$, where ΔT_g is the shift of the glass temperature between measurements performed at two different frequencies ($\Delta \log_{10}(f)$). For typical glass systems like CuMn, AgMn…, the calculated K value is around 0.006, while for super-paramagnetic systems, larger values are found (typically $K \geq 0.1$). Our experimental results give an average value of $K = 0.06$, which is not very revealing for the choice between the two hypotheses. However, a least-squares fit using the power law (= Eq. [1]), or the Arrhenius law (Eq. [2]), seems to indicate that hypothesis for a super-paramagnetic behavior (= interactions between magnetic 'grains') appears the more credible one.

MÖSSBAUER SPECTROSCOPY OF THE Sr–Fe COMPOUND

Mössbauer spectra were obtained with a constant acceleration automatic folding Elscint-type spectrometer using a room temperature ^{57}Co source in transmission geometry; Fe_α was used as a standard reference. Spectra were computed with a least-squares routine using Lorentzian lines. Unlike the misfit compound $(Pb_2FeS_3)_{0.58}NbS_2$ previously described (8), a temperature-dependence study of the Mössbauer spectra has been possible.

At room temperature, the resulting spectrum is non-symmetrical and fitted with one quadrupole doublet whose isomer shift δ is 0.32 mm s^{-1} (see Fig. 8a). This value is in agreement with isomer shifts reported in the case of Fe^{3+} in tetrahedral sulfur environments (0.23 mm s^{-1} in Fe_2S_3 (20), 0.30 mm s^{-1} in $(Pb_2FeS_3)_{0.58}NbS_2$ (8)). It is lower than that observed in $Fe_{1+x}Nb_{3-x}Se_{10}$ (0.50 and 0.46 mm s^{-1}) corresponding to Fe^{3+} in octahedral environment (21, 22). The hypothesis of the presence of iron in a 2+ oxidation state has been considered, but the values of the isomer shift are very different, either in a tetrahedral ($BaFeS_3$: $\delta = 0.41$ mm s^{-1}, $FeNb_2S_4$: $\delta = 0.77$ mm s^{-1} (23, 24)) or in an octahedral environment (FeS: $\delta = 0.83$ mm s^{-1}, $FePS_3$ $\delta = 0.87$ mm s^{-1} (25, 26)). The iron site is very distorted, but this is mainly due to the statistical distribution of sulfur atoms.

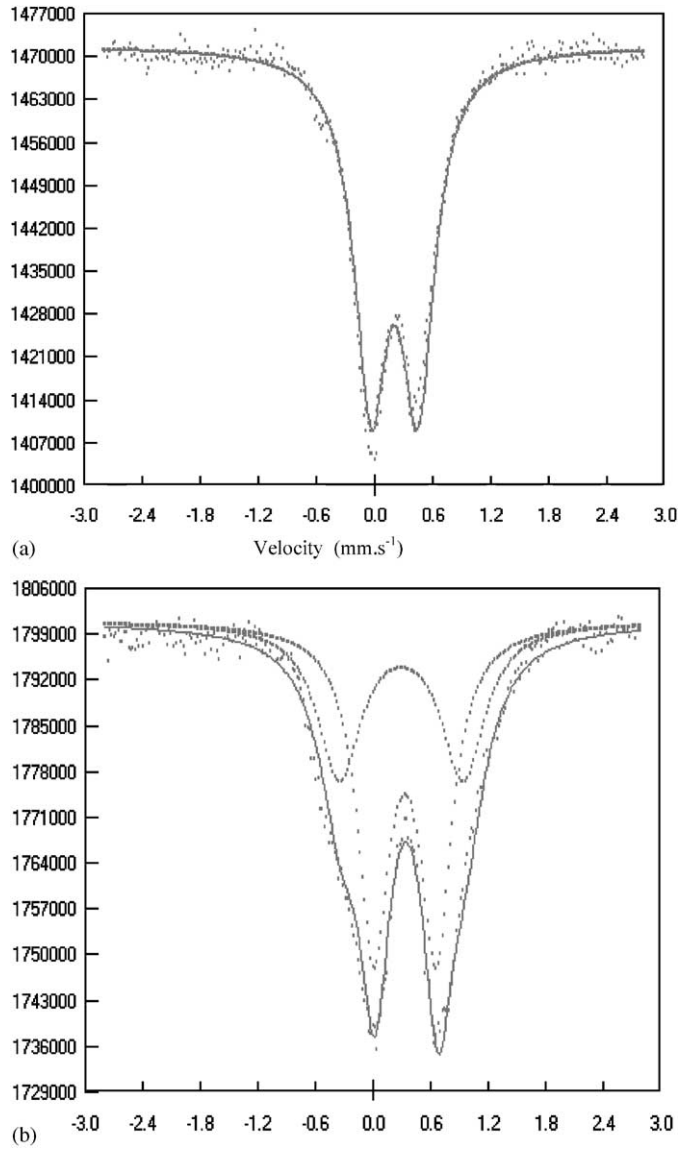

FIG. 8. Mössbauer spectra recorded at $T = 293$ K (a), and $T = 77$ K (b).

In a first approximation the spectrum recorded at 77 K (Fig. 8b) can be fitted with a quadrupole doublet, $\delta = 0.44$ mm s^{-1}, and a quadrupole splitting $\Delta E = 0.81$ mm s^{-1}. But in fact, a shoulder is clearly visible on the spectrum and for this reason it must be fitted with the superposition of two quadrupole doublets whose intensity ratio is roughly $\frac{4}{1}$, with the same isomer shift (0.44 mm s^{-1}) but with different quadrupole splittings (0.71 and 1.48 mm s^{-1}) (see Table 8).

TABLE 8
Mössbauer Parameters in mm s^{-1}

T (K)	Site	δ	ΔE	W	(%)
300	—	0.32	0.48	0.19	100
77	1	0.45	0.71	0.23	80
	2	0.44	1.48	0.21	20

Note. δ, isomer shift (Fe_α as reference), ΔE, quadrupole splitting $=\frac{1}{2}eV_{zz}Q(1+\eta^{2/3})^{1/2}$, W half-linewidth at half-height.

Between room temperature and 77 K, the isomer shift follows a classical linear behavior. Due to the complexity of the structure, a slight change in the distances or the angles in the first coordination shell of iron can easily explain this evolution. This hypothesis is reinforced by the fact that, at 77 K, the spectrum is symmetrical; that corresponds to an evolution of some bonds around the Mössbauer nucleus. In other respects, if the asymmetry observed at 300 K was due to a preferential orientation of the sample, a temperature-independent behavior would be observed. Moreover, an important characteristic of the Mossbauer spectroscopy is the observation time. At room temperature, sulfur atoms are distributed on four statistical positions; only an average value will be observed if the mean life time is shorter than the nuclear precession time ($\tau \approx 10^{-7}$ s). At low temperatures if the exchange is frozen, it will be possible to distinguish several configurations corresponding to different quadrupole splittings.

A valence state estimation based on correspondence between isomer shifts and oxidation states in sulfur environment as proposed by Goodenough and Fatseas (27) leads to a formal valence of $+2.72$; this result has to be considered with caution and as only indicative.

DISCUSSION AND CONCLUDING REMARKS

The studied Sr–Fe and Sr–Gd 1.5Q-misfit derivatives are crystallographically rather similar as their respective magnetic atoms (Fe, Gd) are both located within the central layer of the 1.5Q-part. The only difference in their coordination types, demonstrated from X-ray structure refinement results, is namely a tetrahedral coordination for Fe against an octahedral one for Gd (due to a steric effect between Fe and Gd, as already mentioned in the similar Pb–Fe (8) and Eu–Eu (9) 1.5Q-misfit derivatives). In both compounds, magnetic planes are well separated from each others by five non-magnetic layers, giving grounds to consider them as good examples of 2D-magnetic materials, or at least more illustrative than the $1Q/1H$ homolog for which only three non-magnetic layers are separating adjacent magnetic planes (28).

The Sr–Gd derivative does not present any magnetic transition above 2 K, as predictable for a 2D-material with a rare-earth element as magnetic atom. On the contrary, the Sr–Fe derivative shows a more interesting magnetic behavior attributed to the statistical distribution of Fe atoms over the four close positions surrounding the central site occupied by Nb atoms. This complex situation is even worse when looking at the S atoms within the central layer. Indeed, like for Fe, these S atoms are also distributed over a four split position. This induces a disordered magnetic ion framework, with magnetic interactions of various intensities, giving a very negative θ value. The Curie–Weiss fitting cannot be applied in the temperature range (2–380 K) because of the downward curvature of the inverse susceptibility, which forbids to establish the oxidation state for Fe. To go further in the knowledge about coordination and oxidation state for Fe, an EXAFS study is currently undertaken.

REFERENCES

1. G. A. Wiegers and A. Meerschaut, *Mater. Sci. Forum* **100&101,** 101 (1992).
2. G. A. Wiegers, *Prog. Solid State Chem* 24**,** 1 (1996).
3. A. Guinier, G. B. Bokii, K. Boll-Dornberger, J. M. Cowley, S. Durovic, et al., *Acta Crystallogr. A* **40,** 399 (1984).
4. A. Meerschaut, L. Guemas, C. Auriel, and J. Rouxel, *Eur. J. Solid State Inorg. Chem.* **27,** 557 (1990).
5. Y. Oosawa, Y. Gotoh, J. Akimoto, T. Tsunoda, M. Sohma, and M. Onoda, *Jpn. J. Appl. Phys.* **31,** L1096 (1992).
6. L. M. Hoistad, A. Meerschaut, P. Bonneau, and J. Rouxel, *J. Solid State Chem.* **114,** 435 (1995).
7. A. Lafond, A. Nader, Y. Moëlo, A. Meerschaut, A. Briggs, S. Perrin, P. Monceau, and J. Rouxel, *J. Alloys Compds.* **261,** 114 (1997).
8. A. Lafond, C. Deudon, A. Meerschaut, P. Palvadeau, Y. Moëlo, and A. Briggs, *J. Solid State Chem.* **142,** 461 (1999); C. Deudon, A. Lafond, O. Leynaud, Y. Moëlo, and A. Meerschaut, *J. Solid State Chem.* **155,** 1 (2000).
9. L. Cario, A. Lafond, P. Palvadeau, C. Deudon, and A. Meerschaut, *J. Solid State Chem.* **147,** 58 (1999).
10. STOE-IPDS Software, STOE &Cie (1996).
11. V. Petricek and M. Dusek, "JANA98: Crystallographic Computing System." Institute of Physics, Academy of Sciences of the Czech Republic, Praha, 1998.
12. A. Janner and T. Janssen, *Acta Crystallogr. A* **36,** 408 (1980).
13. P. M. de Wolff, T. Janssen, and A. Janner, *Acta Crystallogr. A* **37,** 625 (1981).
14. S. van Smaalen, *Crystallogr. Rev.* **4,** 79 (1995).
15. S. van Smaalen, *Mater. Sci. Forum* **100&101,** 173 (1992).
16. V. Petricek, K. Maly, P. Coppens, X. Bu, I. Cisarova, and A. Frost-Jensen, *Acta Crystallogr. A* **47,** 210 (1991).
17. R. J. Cava, V. L. Himes, A. D. Mighell, and R. S. Roth, *Phys. Rev. B* **24**(6), 3634 (1981); A. Meerschaut, P. Gressier, L. Guemas, and J. Rouxel, *Mater. Res. Bull.* **16,** 1035 (1981).
18. O. Leynaud, A. Lafond, K. Poduska, and A. Meerschaut, *J. Magn. Magn. Mater.* **231,** 185 (2001).
19. M. Brunner, Diploma Thesis, CRTBT-CNRS, Grenoble, October 1995.
20. A. H. Stillller, B. J. McCormick, P. Russel, and P. A. Montano, *J. Am. Chem. Soc.* **100,** 2554 (1978).

21. R. J. Cava, F. J. Di Salvo, M. Eibschutz, and J. V. Waszczack, *Phys. Rev. B* **27,** 7412 (1983).
22. A. Ben Salem, G. Fatseas, P. Molinié, and A. Meeerschaut, *Synth. Methods* **25,** 207 (1988).
23. N. Nakayama, K. Kasuge, S. Kachis, T. Shinjo, and T. Takada, *J. Solid State Chem.*, **33,** 351 (1980).
24. M. Eibshutz, E. Hermon, and S. Shtrikman, *J. Phys. Chem. Solids* **28,** 1633 (1967).
25. J. L. Horwood, M. G. Townsend, and A. H. Webster, *J. Solid State Chem.* **17,** 35 (1976).
26. B. E. Taylor, J. Steger, and A. Wold, *Solid State Chem.* **7,** 461 (1973).
27. J. B. Goodenough and G. A. Fatseas, *J. Solid State Chem.* **41,** 1 (1982).
28. O. Pena, P. Rabu, and A. Meerschaut, *J. Phys.: Condens. Matter* **3,** 9929 (1991).